13th International Symposium on Turbulence and Shear Flow Phenomena (TSFP13)
Montreal, Canada, June 25–28, 2024

THE EFFECT OF PERMEABILITY ON WAKE CHARACTERISTICS BEHIND STRUCTURED POROUS CYLINDERS

Chansoo Seol
Department of Mechanical System Design Engineering
Seoul National University of Science and Technology
232, Gongneung-ro, Nowon-gu, Seoul, 01811, South Korea
seemsujim@seoultech.ac.kr

Taewoo Kim
Department of Mechanical System Design Engineering
Seoul National University of Science and Technology
232, Gongneung-ro, Nowon-gu, Seoul, 01811, South Korea
taewoo2022@seoultech.ac.kr

Taehoon Kim
Department of Mechanical System Design Engineering
Seoul National University of Science and Technology
232, Gongneung-ro, Nowon-gu, Seoul, 01811, South Korea
tkim99@seoultech.ac.kr

ABSTRACT

This study experimentally investigates the wake structure of a porous square cylinder, emphasizing permeability across a broad range of Da (i.e., $2.4 \times 10^{-5} < Da < 2.9 \times 10^{-3}$). With a simple cubic lattice configuration, the cylinder was produced using advanced additive manufacturing techniques. By combining this technique with a periodic and scalable lattice design, permeability was effectively separated from porosity, allowing for an in-depth parametric study. The primary parameter, permeability, was determined by measuring the pressure drop and superficial velocity for each porous disk within an open-loop pipe flow system. Standard planar particle-image velocity (PIV) measurements in an open-loop wind tunnel captured downstream wake characteristics. The data provided insights into structural alternation in the near-wake related to permeability, revealing four distinct flow regimes based on Da. Additionally, the internal flow adjustment length (L_i) was examined by incorporating a permeability-based source term into the momentum equation, leading to the development of an analytical model for L_i. The experimental results validate this model, highlighting L_i as a characteristic length scale in the near-wake.

Introduction

Flow past a porous body with an infinite length has been often encountered in both engineering and environmental contexts (i.e., aircraft landing gear, river ecosystems, etc.). In this context, the wake structure is primarily governed by two parameters: porosity and permeability, which are intrinsically linked, reflecting the geometric features of the internal porous structure. Although they are intertwined, porosity is frequently used as the primary control parameter in experiments to modify the aerodynamic/hydrodynamic properties of the porous cylinder, due to its ease of manipulation.

Open-cell foam, which is preferred for its consistent global porosity despite its complex internal structure, has often been used to coat cylinders, effectively reducing drag and noise (Klausmann & Ruck, 2017). Recent studies utilizing two-dimensional porous bodies with uniform and organized structures have provided better insights into the role of porosity in wake manipulation. For instance, Steiros *et al.* (2021) employed PIV measurements to study flows past perforated plates with varying porosities, formulating an analytical model that describes the dynamics of downstream recirculation bubbles in both laminar and turbulent states. Through direct numerical simulation (DNS), Nicolle & Eames (2011) revealed the impact of porosity on the downstream wake pattern, identifying three distinct flow regimes. In a different study, Rominger & Nepf (2011) experimentally explored flow adjustments both upstream and within two-dimensional cylinder patches, inspired by emergent vegetation. By properly scaling the momentum equations, they formulated a new parameter, the canopy drag length scale, defined as a product of the cylinder drag and the frontal area density, $(C_Da)^{-1}$. They revealed that this parameter correlates with the flow deceleration, and they proposed an analytical model to describe both upstream and interior flow adjustment length with respect to $(C_Da)^{-1}$.

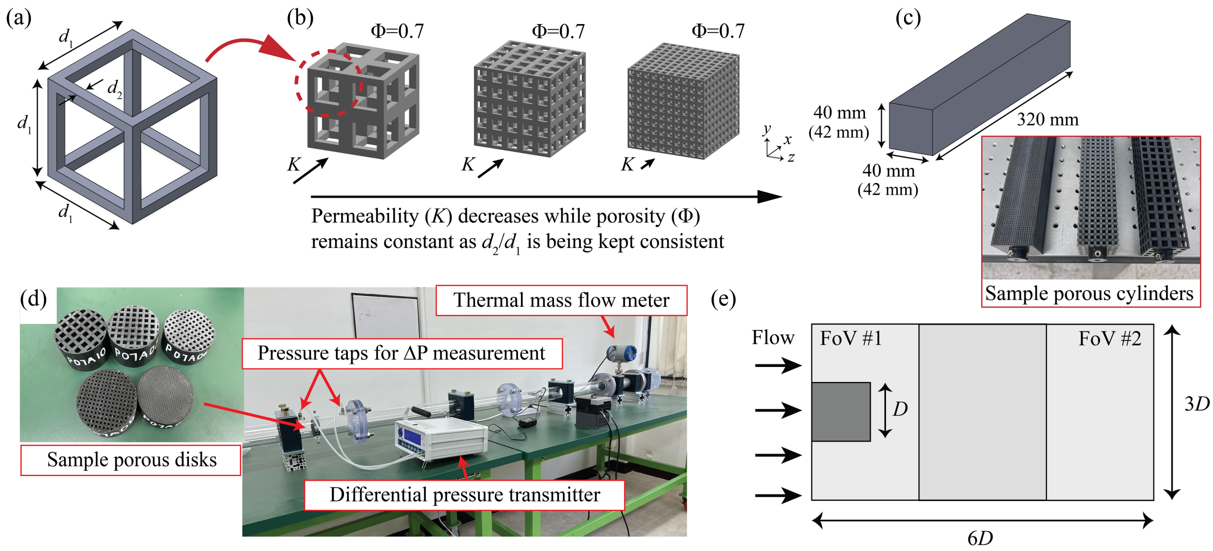

Figure 1. (a) Simple cubic lattice structure as a base porous structure; (b) schematic illustration of decoupling process of permeability from porosity; (c) examples of the current porous square cylinder; (d) experimental setup of the permeability measurement and its sample porous disks; (e) schematic representation of the PIV measurements

Subsequent studies on a circular cylinder patch further confirmed the relationship between downstream flow patterns and the cylinder drag length scale (Chen *et al.*, 2012, 2013).

Despite numerous experimental efforts, the structural modification underlying a two-dimensional porous cylinder remains elusive, due mainly to the intertwined nature of porosity and permeability. In contrast, numerical studies can effectively isolate these parameters, offering deeper insights into the role of permeability in wake dynamics. Cummins *et al.* (2017) conducted numerical simulations (DNS) to investigate flow past porous disks across a broad range of Da ($10^{-9} < Da < 1$), where $Da = K/D^2$ (K is the permeability and D is the cylinder width), in a laminar state. They discovered a direct correlation between Da and the downstream flow patterns, identifying several distinctive flow regimes with respect to Da. Further, Ledda *et al.* (2018) examined the wake structure and its instability at low Reynolds numbers ($Re = U_oD/\nu$, where U_o is the upstream velocity and ν is the kinematic viscosity), highlighting the stronger influence of permeability compared to porosity on flow patterns, as it predominantly affects the force and frequency of the oscillating wake.

While significant advances have been made in understanding the wake dynamics of two-dimensional porous cylinders, a notable knowledge gap persists. Many experimental studies have yet to use permeability as a primary control parameter due to the challenges in creating complex porous models. Some studies (Rominger & Nepf, 2011; Chen *et al.*, 2012) have employed a non-dimensional flow-blockage parameter (C_DaD) resulting from the drag length scale as a representation of permeability. However, this approach serves as an indirect measure. On the other hand, despite their potential for in-depth analysis, numerical studies often restrict themselves to low Re due to high computational costs, leaving the permeability effect at higher Re largely unexplored.

In this study, we take the first experimental attempt to investigate the influence of permeability on the wake structure of porous cylinders at high Reynolds numbers ($Re \sim O(10^4)$). We have fabricated various porous square cylinders whose base structure consists of a periodic and scalable lattice. Utilizing a high-resolution 3D printing technique, we successfully isolated the permeability from porosity, allowing a systematic study of the wake structure behind the porous cylinders in relation to permeability. Detailed permeability, drag, and particle-image velocimetry (PIV) measurements were conducted for the porous cylinders over a wide range of Da. Based on the experimental data, we first examine the evolution of wake structure as it relates to Da. Subsequently, we propose a new analytical model to estimate the interior flow adjustment length with respect to the cylinder permeability and validate it using experimental data.

Experiments

The porous cylinders in this study employ a simple cubic lattice structure characterized by the length of the unit cell (d_1) and the strut width (d_2). As illustrated in figure 1a, this design ensures isotropic permeability, with its porosity (ϕ) determined by the ratio $d_1/2d_2$. Notably, when d_1 decreases while preserving the ratio d_2/d_1, permeability (K) decreases, even though porosity remains consistent. This unique aspect enables us to isolate the impact of permeability on the flow structure of the porous cylinder, separate from porosity effects. Advanced stereolithography (SLA) 3D printing techniques allow the precise fabrication of these complex designs with excellent surface quality.

For this study, we employed 2D square cylinders due to their compatibility with the Cartesian coordinate system. Specifically, 2D cylinders with rectangular cross-sections, in contrast to those with circular ones, are better suited to manipulate the permeability, given the tensor nature. For simplicity, we set the aspect ratio of the rectangular cross-section to 1, yielding a square shape. All the cylinders, whether porous or solid, were fabricated using the SLA 3D printer (Anycubic Photon Mono X), using a width D of 40-42 mm and a length of 320 mm, as represented in figure 1c. Detailed design specifications and attributes of each cylinder can be found in table 1 and in our previous experiment (Seol *et al.*, 2023).

For permeability measurements, we employed an open-

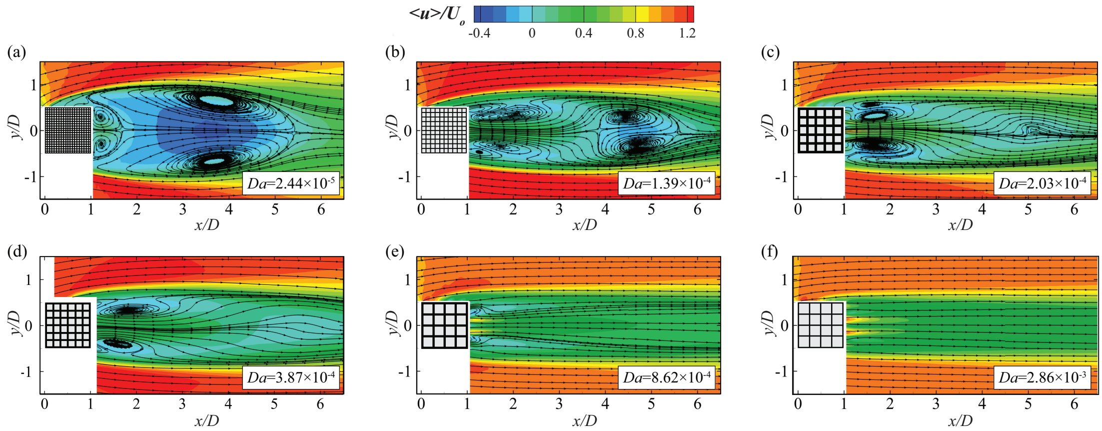

Figure 2. Contour maps of mean longitudinal velocity superimposed with streamlines for each case. Schematic representation of the porous cylinders was included at the origin to give a better understanding of cylinder cross-section and flow patterns depending on the pore size.

loop acrylic pipe of 3.5 m length and 65 mm diameter, as shown in figure 1d. Using advanced 3D printing techniques, porous disks replicating the lattice structures in our study were fabricated with thicknesses varying from 20 mm to 60 mm. This design ensured pressure drops below 2000 Pa at a superficial velocity (U_s) of 15 m/s. The porous disk was positioned 1.2 m from the inlet, and the pressure drop (ΔP) was acquired using a high-resolution pressure transmitter (FCO560, Furness Control). Thus, the permeability of each porous disk was estimated by applying a linear regression on the profile of ΔP versus U_s, based on the Forchheimer equation.

Drag and particle-image velocimetry (PIV) experiments were taken in an open-loop wind tunnel facility at Seoul National University of Science and Technology. This tunnel features a 0.35 m x 0.35 m x 2 m test section. Cylinders were positioned 1 m from the inlet, and drag measurements were conducted using a three-component balance unit (AFA3, TecQuipment). PIV measurements were performed for all cylinder cases, with an upstream speed of 11.5 m/s (or $Re \sim 3.1 \times 10^4$). Measurements were taken at two streamwise locations in the $x-y$ plane to capture long wake structures from the cylinders using two 12 MP TSI Powerview cameras ($4k \times 3k$, 8-bit) equipped with 105 mm Nikkor lenses, providing a $6D \times 3D$ field of view (see figures 1e).

Results

Figure 2 displays selected contour maps of the mean longitudinal velocity, superimposed with streamlines that represent a characteristic downstream flow pattern with respect to permeability. The coordinate system was normalized by the cylinder width, D, and a schematic representation of the porous cylinders is included at the origin to facilitate a better understanding of the cylinder cross-section and the flow patterns depending on the pore size. In figure 2, the longitudinal bleeding flow, observed along the symmetric plane in all porous cases is significantly influenced by the permeability of the cylinder, which alters the downstream wake structure. As Da increases, the bleeding flow extends, pushing the primary recirculation bubble further downstream and reducing its size (Cummins *et al.*, 2017; Ledda *et al.*, 2018). At a critical point ($Da_{c1} = 2.0 \times 10^{-4}$), as depicted in figure 2c, the reverse flow disappears and is replaced by a positive and constant velocity region that indicates a steady wake (Zong & Nepf, 2012).

Table 1. Parameters for the structured porous square cylinders. ϕ: porosity; d_1: length of the unit cell; d_2: strut width; D: cylinder width; $L_{i,exp}$: downstream adjustment length from the measurements; Da: Darcy number.

Case	Φ	d_1 (mm)	d_2 (mm)	D (mm)	$L_{i,exp}/D$	Da ($\times 10^{-4}$)
S	0	–	–	40	–	–
A1	0.7	2.0	0.36	40	0.68	0.24
A2	0.7	4.0	0.73	40	2.02	0.64
A3	0.7	6.0	1.09	42	2.65	0.97
A4	0.7	8.0	1.45	40	3.74	2.03
A5	0.7	10.0	1.82	40	4.73	4.07
B1	0.8	2.0	0.29	40	1.47	0.58
B2	0.8	4.0	0.57	40	2.87	1.39
B3	0.8	6.0	0.86	42	3.95	2.17
B4	0.8	8.0	1.15	40	4.81	4.17
B5	0.8	10.0	1.44	40	5.52	8.62
C1	0.9	2.0	0.20	40	3.32	1.09
C2	0.9	4.0	0.39	40	4.67	2.30
C3	0.9	6.0	0.59	42	–	7.16
C4	0.9	8.0	0.78	40	5.58	16.8
C5	0.9	10.0	0.98	40	4.86	28.6

When Da becomes sufficiently high (see figure 2f), a second pair of recirculation bubbles attached to the trailing edge of the porous cylinder completely disappears, indicating the predominance of small-scale vortices that shed from the individual lattices (Nicolle & Eames, 2011; Seol *et al.*, 2023). This transition marks another critical Darcy number, $Da_{c2} = 1.0 \times 10^{-3}$.

The downstream flow adjustment length L_i represents the distance from the leading edge of the porous media to the location where the flow pressure balances with the drag encountered as the flow passes through the porous media (Rominger & Nepf, 2011). In the context of flow past a single porous cylinder, this adjustment length plays a role as a characteristic length scale for the mean longitudinal velocity along the cylinder center (Zong & Nepf, 2012; Chen *et al.*, 2012). Here, we propose an analytical model to assess the downstream flow adjustment length, leveraging the governing equations. Utilizing the Darcy-Brinkman-Forchheimer extended model, we specify the governing equations for the longitudinal and lateral momentum to describe the flow within the porous region (Chen *et al.*, 2008; Yu *et al.*, 2010). To determine the downstream adjustment length L_i, the governing equations are scaled using the following characteristic values: $x = L_i$, $y = D/2$, $u = U_e$, $v = DU_e/2L_i$, and $\partial p/\partial x \sim \Delta p/L_i$. Then scaled equations are further simplified by dividing each by the inertial term as

$$1 \sim -\frac{\Phi^2 \Delta p}{\rho U_e^2} - \Phi^2 F \left[\left(\frac{L_i}{\sqrt{K}} \right)^2 + \left(\frac{D}{2\sqrt{K}} \right)^2 \right]^{1/2} \quad (1)$$

$$1 \sim -\frac{4\Phi^2 L_i^2 \Delta p}{\rho D^2 U_e^2} - \Phi^2 F \left[\left(\frac{L_i}{\sqrt{K}} \right)^2 + \left(\frac{D}{2\sqrt{K}} \right)^2 \right]^{1/2} \quad (2)$$

In scaling the pressure term in 1 and 2, a dual scaling approach is adopted, as suggested by Rominger & Nepf (2011). The change in kinetic energy ($\Delta p/\rho U_e^2 = (\rho U_e^2 - \rho \langle u \rangle_{x=0}^2)/\rho U_e^2$), which represents the pressure change at the leading edge, is found to be logarithmically proportional to Da (not shown for brevity). Therefore, the scaling $\Delta p/\rho U_e^2 \sim \log(1/2\sqrt{Da})$ is applied to cases with low flow-blockage ($Da > Da_{c1}$), while $\Delta p/\rho U_e^2 \sim 1$ applies to cases with high flow-blockage ($Da < Da_{c1}$)).

Building on the aforementioned dual scaling for the pressure term, the length scale of the downstream adjustment region for low flow-blockage (L_{i1} for $Da < Da_{c1}$)) and high flow-blockage (L_{i2} for $Da > Da_{c1}$) can now be expressed as

$$L_{i1} \sim 7\sqrt{K} \left[1 + \log\left(\frac{1}{2\sqrt{Da}} \right) \right] \quad (3)$$

$$L_{i2} \sim 7\sqrt{K} \left[\frac{1}{\Phi} + \left(\frac{1}{14\sqrt{Da}} \right)^2 \right]^{1/2} \quad (4)$$

Figure 3 presents the downstream flow adjustment length as a function of the modified non-dimensional parameter $\sqrt{Da_{c1}}/\sqrt{Da}$, obtained from analytical models (1 and 2). This figure features dashed and dashed-dot lines, representing data calculated from the analytical model for low and high flow-blockage cases, respectively. For comparison, experimental data on flow adjustment length ($L_{i,exp}$) are also plotted in figure 3. Specifically, $L_{i,exp}$ for high flow-blockage cases is defined as the distance from the trailing edge of the cylinder to the first stagnation point behind the cylinders. In contrast,

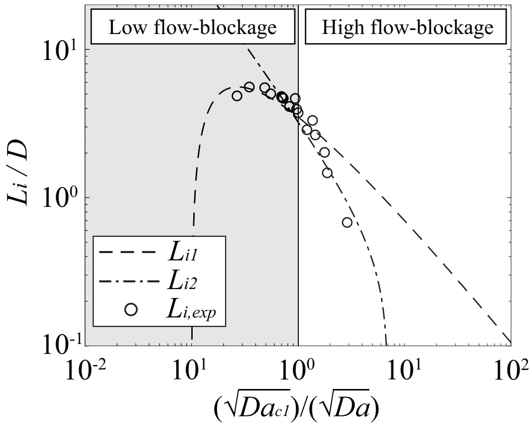

Figure 3. downstream flow adjustment length over the modified non-dimensional parameter $\sqrt{Da_{c1}}/\sqrt{Da}$. L_{i1} and L_{i2} are obtained from the analytical model (3-4) for the low and high flow-blockage cases, respectively. $L_{i,exp}$ is measured data.

for low flow-blockage case, $L_{i,exp}$ represents the distance to the point where the gradient of centerline velocity decrease falls below $\partial(U/U_o)/\partial(x/D) < -0.1$. Detailed methodology for determining $L_{i,exp}$, based on PIV measurements, was discussed in our prior work (Seol *et al.*, 2023).

As shown in figure 3, there is excellent agreement between the experimental result and the analytical model across the entire permeability range examined. Notably, the analytical model (3) for low flow-blockage cases shows a local maximum in L_{i1}, followed by a decrease as $\sqrt{Da_{c1}}/\sqrt{Da}$ decreases, aligning with the experimental observations. Conversely, L_{i2} for high flow-blockage cases declines sharply with an increase in $\sqrt{Da_{c1}}/\sqrt{Da}$, closely matching the experimental data.

In investigating the role of the downstream flow adjustment length as a characteristic length scale in the flow past porous cylinders, mean longitudinal velocity profiles along the cylinder centerline were examined using different normalization methods (figures 4a and 4b). Figure 4a displays profiles normalized by cylinder diameter D, revealing significant dispersion among the profiles, suggesting D is not an appropriate scale for characterizing velocity immediately behind the cylinder. Conversely, figure 4b, which normalizes profiles by the downstream adjustment length $L_{i,exp}$ derived from measurements, shows a close alignment of velocity profiles, indicating a uniform flow adjustment behavior in the near wake. This alignment highlights L_i as an appropriate scaling parameter for flow adjustment, consistent with prior experimental observations (Zong & Nepf, 2012; Chen *et al.*, 2012, 2013).

Conclusion

In this study, we investigated the impact of permeability on the wake characteristics of the porous square cylinders. The permeability was systemically decoupled from porosity by utilizing a periodic and scalable lattice structure, fabricated by using high-resolution 3D printing, serving as an isolated control parameter over two decades of Da. This approach allowed the identification of two critical Darcy numbers, from which four distinct flow regimes were classified based on Da. In addition to the wake structure, our findings confirmed a close correlation between the drag induced by the porous cylinder and its permeability, indicating that the pressure drop across the porous cylinder is a function of Da (Yu *et al.*, 2010; Ledda *et al.*, 2018). Based on this observation, the current study re-

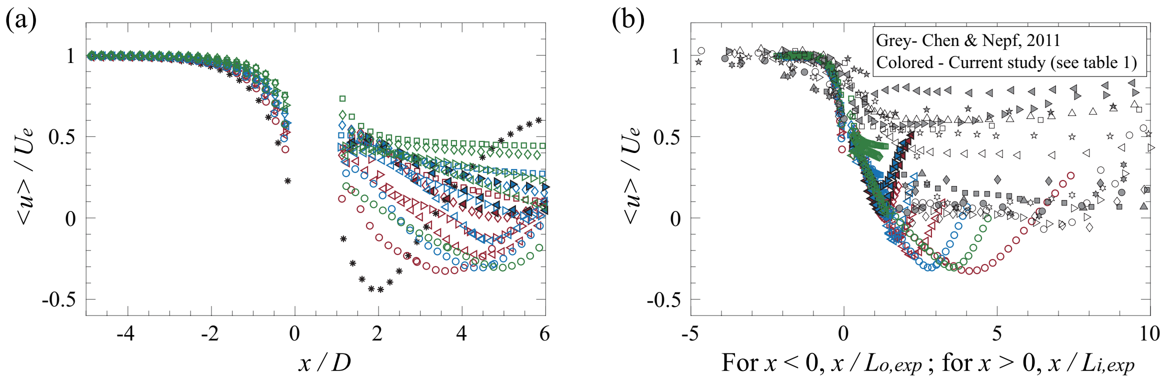

Figure 4. Profiles of mean longitudinal velocity along the centerline, (a) normalized by the cylinder width D and (b) normalized by the measured $L_{i,exp}$ for $x > 0$ and $L_{o,exp}$ for $x < 0$. Symbols for the current study are summarized in table **??**. Grey open and solid symbols are from figure 4 in Chen *et al.* (2012).

visited the method of determining the interior flow adjustment length (L_i), which was previously defined through the cylinder drag and front areal density (Rominger & Nepf, 2011). The present process involved integrating a Darcy-Brinkman-Forchheimer extended model into the momentum equation. As a result, we proposed a new analytical model to evaluate L_i in relation to permeability, and the present experimental data validated this analytical model. Furthermore, L_i was employed to normalize the x-axis of the mean longitudinal velocity profiles at the cylinder center for all porous cases. The result showed an excellent alignment, implying a rapid flow adjustment in the near wake with respect to the L_i. This observation confirms that L_i plays a crucial role as a characteristic length scale for the flow around the porous cylinder and further validated the analytical model for L_i proposed herein.

REFERENCES

Chen, Xiaobing, Yu, Peng, Winoto, SH & Low, Hong-Tong 2008 Numerical analysis for the flow past a porous square cylinder based on the stress-jump interfacial-conditions. *International Journal of Numerical Methods for Heat & Fluid Flow* **18** (5), 635–655.

Chen, Zhengbing, Jiang, Chunbo & Nepf, Heidi 2013 Flow adjustment at the leading edge of a submerged aquatic canopy. *Water Resources Research* **49** (9), 5537–5551.

Chen, Zhengbing, Ortiz, Alejandra, Zong, Lijun & Nepf, Heidi 2012 The wake structure behind a porous obstruction and its implications for deposition near a finite patch of emergent vegetation. *Water Resources Research* **48** (9).

Cummins, C., Viola, I. M., Mastropaolo, E. & Nakayama, N. 2017 The effect of permeability on the flow past permeable disks at low reynolds numbers. *Physics of Fluids* **29** (9).

Klausmann, K. & Ruck, B. 2017 Drag reduction of circular cylinders by porous coating on the leeward side. *Journal of Fluid Mechanics* **813**, 382–411.

Ledda, P. G., Siconolfi, L., Viola, F., Gallaire, F. & Camarri, S. 2018 Suppression of von kármán vortex streets past porous rectangular cylinders. *Physical review fluids* **3** (10), 103901.

Nicolle, A & Eames, I 2011 Numerical study of flow through and around a circular array of cylinders. *Journal of Fluid Mechanics* **679**, 1–31.

Rominger, J. T. & Nepf, H. 2011 Flow adjustment and interior flow associated with a rectangular porous obstruction. *Journal of Fluid Mechanics* **680**, 636–659.

Seol, C., Hong, J. & Kim, T. 2023 Flow around porous square cylinders with a periodic and scalable structure. *Experimental Thermal and Fluid Science* **144**, 110864.

Steiros, K., Bempedelis, N. & Ding, L. 2021 Recirculation regions in wakes with base bleed. *Physical Review Fluids* **6** (3), 034608.

Yu, P, Zeng, Y, Lee, TS, Bai, HX & Low, HT 2010 Wake structure for flow past and through a porous square cylinder. *International Journal of Heat and Fluid Flow* **31** (2), 141–153.

Zong, L. & Nepf, H. 2012 Vortex development behind a finite porous obstruction in a channel. *Journal of Fluid Mechanics* **691**, 368–391.